 CMES, vol.50, no.3, pp.285-303, 2009

Numerical Simulations of Flows over a Pair of Cylinders at Different Arrangements using the Immersed Boundary Method

A.R. da Silva[1], A. Silveira-Neto[2,3], D.A. Rade[2]
R. Francis[4] and E.A. Santos[4]

Abstract: In the context of computational fluid dynamics a numerical investigation of incompressible flow around fixed pairs of rigid circular cylinders was carried out. The two-dimensional filtered Navier-Stokes equations with the Smagorinsky sub-grid scale model were solved using a Cartesian non-uniform grid. The immersed Boundary Method with the Virtual Physical Model was used in order to model the presence of two circular cylinders embedded in the flow. The fractional time step method was used to couple pressure and velocity fields. The simulations were carried out for Reynolds number equal to 72,000 for pitch ratio equal to 2 and different arrangements regarding the relative positions of the cylinders. The flow interference between the two cylinders, the vortex shedding process and the behavior of the dynamic coefficients were investigated. The results of the present study were compared with experimental data from the literature. The Immersed Boundary Method has showed to be efficient in the simulation of flows, taking into account the presence of multi-body compositions.

Keywords: Immersed boundary method, dynamic coefficients, circular cylinders, computational fluid dynamics.

[1] Federal University of Itajubá, Mechanical Engineering Institute, Campus José Rodrigues Seabra - P.O.Box 50, CEP 37500-902, Itajubá-MG - Brazil.
[2] Federal University of Uberlândia, School of Mechanical Engineering, Campus Santa Mônica - P.O.Box 593, CEP 38400-902 - Uberlândia - MG – Brazil.
[3] Corresponding author. Tel.: +55 34 32 39 41 48; Fax: +55 34 32 39 42 06. E-mail address: aristeus@mecanica.ufu.br.
[4] Center of Research of PETROBRAS Submarine Technology - CENPES/PDP/TS, Rio de Janeiro - RJ - Brazil.

1 Introduction

Flows over circular cylinders have been studied by many researchers. For high Reynolds number, the non-linear effects become important and the Linear Stability Analysis (LSA) of the steady-state flow does not predict the correct dimensionless frequency associated to the flow instability [Mittal (2008)]. According to this author the RANS equations with a turbulence model are employed to obtain a time-averaged flow. In these situations, LSA can provide useful information about the stability of these flows. [Liu and Yu (2008)] have considered the flows generated by a circular cylinders moving with a constant velocity. They assumed viscous and incompressible steady flows. For the analyses, they have considered the coupling method of natural boundary element and mixed finite element for stationary Navier-Stokes equations in unbounded domains. The authors observed that increasing the order of the artificial boundary condition and refining the mesh decreases the solutions error.

Flow over a pair of circular cylinders has also been studied and appears in a large number of engineering applications. Depending on the arrangement of these cylinders, relative to the flow, a wide variety of phenomena can be observed. In the present paper a detailed numerical study of the flow over a pair of cylinders in different arrangements is presented. The main goal of the study is to have a better understanding of the flow around a bundle of risers, which are subjected to shear flow due to maritime currents. These risers are used to transport oil to the offshore platforms. The flow around risers is very complex and changes in intensity and direction with the water depth. From the phenomenological point of view, the interference of the flow around bluff bodies is responsible for the changing in the characteristics of the fluid load acting over these immersed bodies. Furthermore, flow over circular cylinders is related to different fundamental fluid-dynamic phenomena, such as boundary-layer separation, shear-layer development and vortex dynamics [Akbari and Price (2005)].

The tandem and side-by-side arrangements are the most extensively studied in the literature [Sumner, Price and Païdoussis (1999), Carmo and Meneghini (2006), Deng, Ren, Zhou and Shao (2006)]. However, the most general form is the staggered arrangement [Sumner, Richards and Akosile (2005)]. According to the literature there are different interference regimes, which have been identified by flow visualization in experimental works. The wake behavior of a pair of cylinders can be classified in groups, according to the pitch ratio. The authors [Sumner, Price and Païdoussis (1999)] have identified three types of behavior based on the pitch ratio. The first type is the behavior which is similar to that observed for a single bluff body, when the cylinders are in contact. In the second type, the recirculation zone has limited growth in the flow direction and has lateral expansion for moder-

ate pitch ratio. The last type exhibits recirculation around each cylinder similar to what is verified for single circular cylinder. Figure 1 illustrates the flow patterns for two circular cylinders of equal diameters in steady cross-flow, for different angles of incidence.

The objective of the present paper is twofold: (i) to apply the Immersed Boundary Methodology to simulate the flow over stationary pair of cylinders; (ii) to analyze the interference effect between the cylinders and to characterize the mechanism of vortex shedding in various configurations. Regarding the simulation results, the vorticity contours and the time histories of lift and the drag coefficients, for Reynolds number equal to 72,000, are presented. The outline of the paper is as follows: we first describe the mathematical model for incompressible flows together with the mathematical methodology in Section 2. In Section 3, we describe the numerical algorithm used and in the Section 4 we present the numerical results. Finally, in Section 5 the concluding remarks are presented.

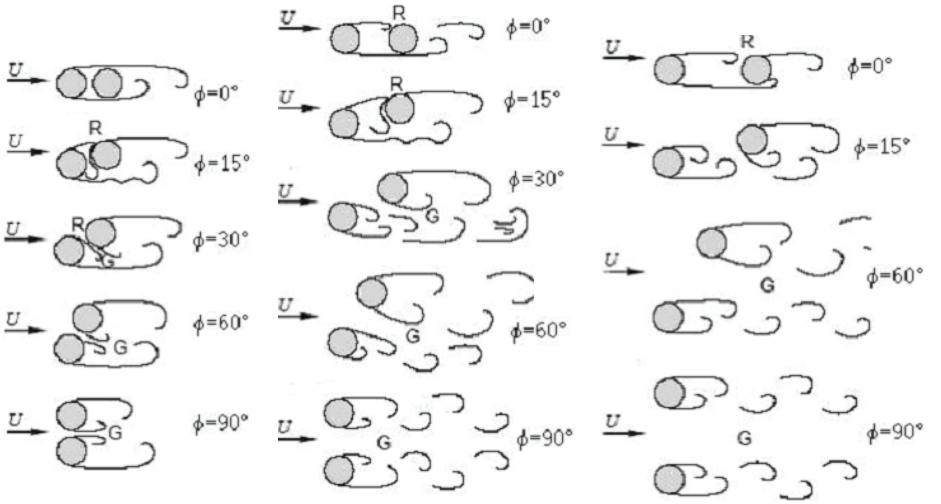

Figure 1: Flow patterns for two circular cylinders of equal diameters: (a) closely spaced; (b) moderately spaced; (c) widely spaced. R is the reattachment and G is the gap (adapted from [Summer, Richards and Akosite (2005)]).

2 Modeling methodology

The methodology used in the present work is based on the Immersed Boundary Method (IBM) [Peskin (1977)] associated with the Virtual Physical Model [Lima e Silva, Silveira-Neto and Damasceno (2003)]. This methodology is based on the Navier-Stokes equations with an added force source term. This force term acts so that the fluid perceives the existence of the immersed body, thus making the exchange of information between both domains. In this methodology a mixed Eulerian-Lagrangean formulation is used, where an Eulerian grid (fixed) describes the flow and a Lagrangean grid (which can be fixed or not) describes the immersed bodies. Figure 2 shows these grids for a two-dimensional domain with an arbitrary interface. These meshes are geometrically independent, which allows the modeling of flows around complex, movable or deformable geometries without the need of any remeshing process. Both domains are physically coupled by a force field obtained at the Lagrangean points, which is then distributed over the Eulerian nodes in the body's neighborhood.

In recent years, the IBM has promoted many researches and applications, as can be cited: problems of fluid-structure interaction [Griffith and Peskin (2005), Lee, Ha, Yoon and Balachandar (2009)], flows over bodies with complex geometry, with arbitrarily movement [Kim and Choi (2006)], fluid-solid flows [Su, Lai and Lin (2007)].

2.1 Mathematical formulation for the fluid

One approach, which is not very common to solve the Navier-Stokes flows, is the so called velocity-vorticity formulation [Nicolás and Bermúdez (2007)]. In this work, the two-dimensional viscous, incompressible flows can be modeled by the filtered Navier-Stokes equations in primitive variables [Báez and Nicolás (2009)], velocity and pressure, as follows:

$$\frac{\partial u_i}{\partial t}+\frac{\partial\left(u_i u_j\right)}{\partial x_j}=-\frac{1}{\rho}\frac{\partial p}{\partial x_i}+\frac{\partial}{\partial x_j}\left[\nu_{ef}\left(\frac{\partial u_i}{\partial x_j}+\frac{\partial u_j}{\partial x_i}\right)\right]+f_i \tag{1}$$

$$\frac{\partial u_i}{\partial x_i}=0 \tag{2}$$

where ρ $[kg/m^3]$ and ν_{ef} $[m^2/s]$ are the specific mass and the effective viscosity, respectively; u_i $[m/s]$ is$i$-th component of the filtered velocity, p $[N/m^2]$ is the filtered pressure, and f_i $[N]$ is the i-th component of the Eulerian vector force, which is calculated by the distribution of the components of the Lagrangean vector force as:

$$f\left(\vec{x}\right)=\sum_k D_{ij}\left(\vec{x}-\vec{x}_k\right)F\left(\vec{x}_k\right)\Delta S^2\left(\vec{x}_k\right) \tag{3}$$

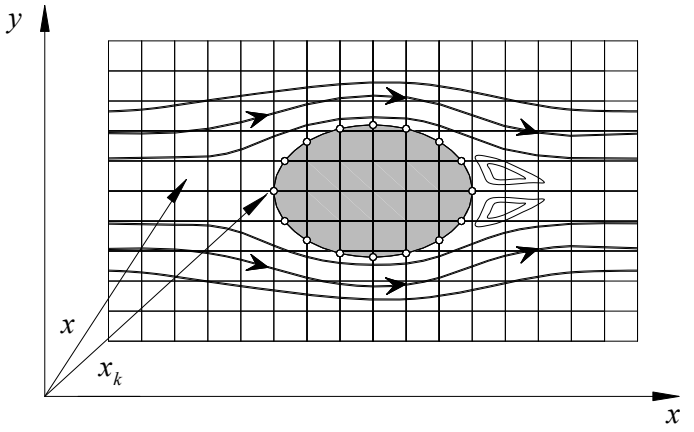

Figure 2: llustration of the Eulerian and Lagrangean meshes.

In Eq. (3) $\vec{x}[m]$ and $\vec{x}_k[m]$ are the position vectors of the Eulerian and Lagrangean points, respectively,$\Delta S[m]$ is the distance between two Lagrangean points as shown in Fig. 3(a), $\vec{F}(\vec{x}_k)[N]$ is the i-th component of the Lagrangean force over the interface, and $D_{ij}[m^{-2}]$ is the interpolation/distribution function proposed by [Peskin and McQueen (1994)].

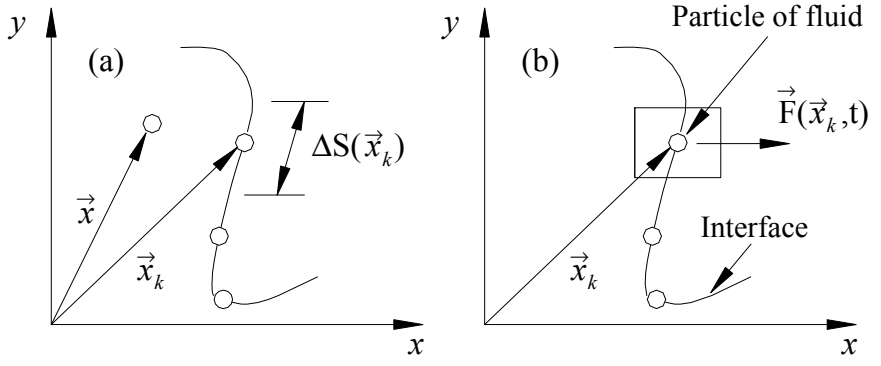

Figure 3: (a) Illustration of the distance between two Lagrangean points and of the vectors $\vec{x}$ and $\vec{x}_k$; (b) illustration of a particle of fluid on the interface.

2.2 Mathematical formulation for fluid-solid interface: the Virtual Physical Model

The Virtual Physical Model enables to calculate the Lagrangean force field based on the momentum balance over a fluid particle placed on the Lagrangean points, as shown in Fig. 3(b). Applying Newton's second law to such a particle of fluid, the Lagrangean force is found to be given by:

$$\vec{F}(\vec{x}_k,t) = \underbrace{\rho\frac{\partial\vec{V}(\vec{x}_k,t)}{\partial t}}_{\vec{F}_a} + \underbrace{\rho\vec{\nabla}\left[\vec{V}(\vec{x}_k,t)\vec{V}(\vec{x}_k,t)\right]}_{\vec{F}_i} - \underbrace{\mu\vec{\nabla}\left[\vec{\nabla}\vec{V}(\vec{x}_k,t)+\vec{\nabla}^T\vec{V}(\vec{x}_k,t)\right]}_{\vec{F}_v} + \underbrace{\vec{\nabla}p(\vec{x}_k,t)}_{\vec{F}_p} \quad (4)$$

where $\vec{F}_a[N]$ is the force engendered by the particle acceleration, $\vec{F}_i[N]$ is the inertial force, $\vec{F}_v[N]$ is the viscous force and $\vec{F}_p[N]$ is the pressure force. These terms are calculated using an approximation based on Lagrange polynomials. Once obtained the force given by Eq. (4), it is distributed to Eulerian nodes according to Eq. (3), in order to obtain the Eulerian force field that accounts for the immersed bodies.

2.3 Turbulence model

The turbulence phenomenon is one of the most challenging problems of modern physics and is among the most complex and fascinating phenomena found in nature. Due to several practical implications in different sectors, the number of research related to understanding and control of turbulent flow has increased dramatically. According to [Vertnik and Šarler (2009)] those flows could be well predicted by the direct numerical simulation (DNS), but only for low Reynolds number. In their work, a low-Re $k-\varepsilon$ model was used for the solution of incompressible turbulent flow by a mesh-free method. The suitability of various turbulence models was also investigated for highly complex swirling flows in tangential inlet cyclones [Karagoz and Kaya (2009)]. In the present paper, the turbulence model used is based on the filtering process, using the so-named box filter. The turbulent viscosity is given as a function of the strain rate and of the scale length as [Smagorinsky (1963)]:

$$v_t = (C_s l)^2\sqrt{2\bar{S}_{ij}\bar{S}_{ij}} \quad (5)$$

where the strain rate $\bar{S}_{ij}$ is given as follows:

$$\bar{S}_{ij} = \frac{1}{2}\left(\frac{\partial\bar{u}_i}{\partial x_j}+\frac{\partial\bar{u}_j}{\partial x_i}\right) \quad (6)$$

where $l = \sqrt{\Delta x \Delta y}$ is the characteristic sub-grid length, and C_s is the Smagorinsky constant. The analytical value for homogeneous and isotropic turbulence is $C_s = 0.18$. Here, the sub-grid turbulent viscosity plays the role of stabilizing the numerical instabilities. In the present work, these instabilities are characteristics of the central difference scheme, which is used for both advective and diffusive terms.

In all simulations a damping function was used in the outlet of the domain. This function absorbs the vortex in the outlet, avoiding reflections that could propagate from the outlet towards the inlet of the domain. This function is given by [Meitz and Fasel (2000)]:

$$g(\varepsilon) = 1 - 6\varepsilon^5 + 15\varepsilon^4 - 10\varepsilon^3 \tag{7}$$

with:

$$\varepsilon = \frac{i - i_1}{i_2 - i_1} \tag{8}$$

where i is the grid number. The points i_1 and i_2 ($i_1 \leq i \leq i_2$) indicate the initial and final grid points of the damped zone. This damping function has the form shown in Fig. 4.

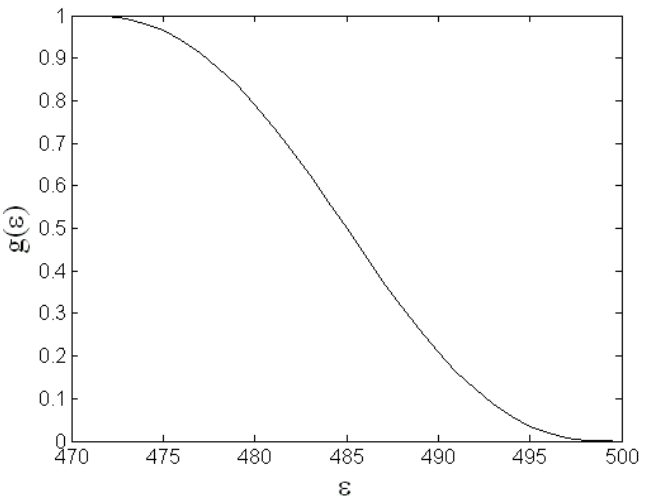

Figure 4: Damping function.

3 Discretization method

A number of mesh-free methods have been developed [Vertnik and Šarler (2009)] in recent years, to circumvent the polygonisation problem found in the classical numerical methods. Here, the momentum and continuity equations are numerically solved using the finite difference method through the fractional step method based on the pressure correction concept [Chorin (1968)]. Given the initial velocity, the pressure and the force fields, an estimated velocity field is obtained. These velocity field is used to calculate the pressure correction, solving a system of linear algebraic equations, for which the *MSI* (Modified Strongly Implicit Procedure), developed by [Scheneider and Zedan (1981)], is used. The Poisson equation gives the coupling between Eqs. (1) and (2). Also, it provides values of pressure that allow that the velocities components, obtained using the Navier-Stokes equations, satisfy the mass conservation condition. The time discretization is done by the second order Runge-Kutta method. The estimation of the velocity is calculated as:

$$\frac{\tilde{u}_i^{n+1}-u_i^n}{\Delta t}=-\frac{1}{\rho}\frac{\partial p^n}{\partial x_i}-\left[\frac{\partial\left(u_iu_j\right)}{\partial x_j}\right]^n+\frac{\partial}{\partial x_j}\left[v_{ef}\left(\frac{\partial u_i}{\partial x_j}+\frac{\partial u_j}{\partial x_i}\right)\right]^n+f_i^n \tag{9}$$

where $\tilde{u}_i$ $[m/s]$ is the estimated velocity component, Δt $[s]$ is the computational time step and n is the substep index. The Poisson equation for pressure correction, $p^{'n+1}$, with the source term given by the divergent of the estimated velocity, is given by:

$$\nabla^2 p^{'n+1}=\frac{\rho\vec{\nabla}\vec{\tilde{u}}^{n+1}}{\Delta t} \tag{10}$$

The velocity field is updated by solving the following equation:

$$u_i^{n+1}=\tilde{u}_i^{n+1}-\frac{\Delta t}{\rho}\frac{\partial p^{'n+1}}{\partial x_i} \tag{11}$$

The previous pressure field p^n and the correction pressure $p^{'n+1}$ are used to calculate the updated values of the pressure field, according to:

$$p^{n+1}=p^n+p^{'n+1} \tag{12}$$

4 Numerical results

In the present study, the cylinders are assumed to have equal diameters d and the distance between their centers is designated by$P$for all configurations (tandem, side-by-side and staggered). The incidence angle between the flow direction and

the line connecting the centers of the cylinders is indicated by ϕ. Figure 5 presents the configurations used herein: Fig. 5(a) depicts the tandem arrangement; Fig. 5(b) indicates the staggered arrangement, in which the upstream cylinder is fixed, while the downstream cylinder position defines the incidence angle $0^\circ < \phi < 90^\circ$; and Fig. 5(c) illustrates the side-by-side arrangement. In all the simulated cases, the pair of cylinders is symmetrically placed in a uniform grid. The distance from the surface of each cylinder to the borders of the uniform region is $1.25d$ in the x direction and $2d$ in y direction.

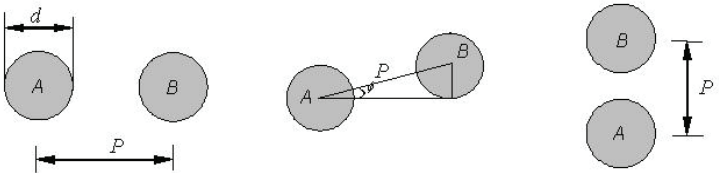

Figure 5: Scheme of the two cylinders: (a) tandem arrangement ($\phi = 0^\circ$); (b) staggered arrangement ($0^\circ < \phi < 90^{circ}$); (c) side-by-side arrangement ($\phi = 90^\circ$).

The simulations were performed at Reynolds numbers $Re = 72,000$. The dimensionless time was defined as $T = tU/d$, where t [s] is the physical time. The time step was set as $\Delta t = 1 \times 10^{-5}$[s] at the first iteration and was increased gradually up to $\Delta t = 1 \times 10^{-3}$[s] during the first 100 iterations. After that, the time step was calculated so that the stability criterion is attained. The grid used is 600x300 points in x and y directions, respectively.

4.1 Characteristics of vortex shedding

In order to investigate the effect of the cylinders proximity on vortex shedding, simulations were performed for cylinders in tandem, staggered and side-by-side arrangements. For all cases, the pitch ratio was assumed to be $P/d = 2$. The vorticity contours shown in Fig. 6 put in evidence very interesting characteristics of the flow as the incidence angle changes. In Fig. 6(a) it can be observed that for the tandem arrangement, the shear layers of cylinder A involves cylinder B with only one vortex wake formed behind the downstream cylinder. The interaction between the two shear layers occurs only behind cylinder B, which is inside the wake of cylinder A. There is a '2S' mode of vortex shedding, composing the classical Von Kármán Street. According to [Naudascher and Rockwell (1994)], vortex shedding behind the upstream cylinder (in the present case cylinder A) is not perceived for pitch ratios smaller than 3.8. For low Reynolds number ($Re = 220$),

[Deng, Ren, Zhou and Shao (2006)], concluded that for two-dimensional simulations, each cylinder yielded a vortex wake only for $P/d \geq 4$. They also stated that, even in three-dimensional flows for this configuration and $P/d \leq 3.5$, the flow is quasi two-dimensional. For$7^\circ < \phi < 15^\circ$, the internal shear layer from the upstream cylinder collides with the frontal part of the downstream cylinder. As the incidence angle increases, the vortex wake becomes irregular behind the cylinder B. For $\phi = 7^\circ$, the '2S' mode of vortex shedding is observed. Increasing the angle ϕ, vortices pairs as well as single vortices are observed, composing the wake, as shown in Fig. 6(d). From Figs. 6(f) to 6(i) it is observed a different behavior of the flow. In the region near the cylinders, two wakes are formed: the wake from cylinder A is narrow, while the wake from the cylinder B is wide. However, it is not possible to classify the vortex shedding mode. The wake becomes complex and disorganized. It should be noted that these vorticity fields are qualitatively similar to the standard behavior presented in Fig. 1.

Simulations have also been performed with two circular cylinders in a side-by-side arrangement for the same pitch ratio and the same Reynolds number. In this configuration, the line defined by the centers of the two cylinders is oriented perpendicularly to the oncoming flow. For this case, the classification of vortex shedding in phase or anti phase, adopted in the present work, is the same used by [Wang and Zhou (2005)]. This classification is illustrated in Fig. 7. An anti-phase wake, with symmetric vortex shedding around the central line of the flow, can be observed in Fig. 6(j). As time passes, it is observed a gap between the two wakes at approximately $10d$ downstream of the cylinders. Anti-phase wake was also observed by other authors at other Reynolds number and pitch ratio. [Wang and Zhou (2005)] verified this behavior for pitch ratio equal to 3 and $Re = 5,900$. According to those authors, the anti-phase vortex shedding is relatively stable, while the in-phase vortex shedding mode is unstable.

4.2 Drag and lift coefficients

Figure 8 shows the time histories of the drag coefficient C_d for the upstream cylinder.

It can be seen that the values of this coefficient do not experience large changes in magnitude for $\phi \leq 60^\circ$. However, the fluctuations increase considerably and become more irregular for $\phi = 75^\circ$. For $\phi = 90^\circ$ the signal becomes periodic.

Figure 9 shows the time histories of the drag coefficient for the downstream cylinder, whose amplitudes, for low incidence angles ($\phi \leq 30^\circ$) are slightly greater than the amplitudes obtained for the upstream cylinder.

For $\phi = 45^\circ$ and $\phi = 60^\circ$, the drag fluctuations for both cylinders exhibit the same

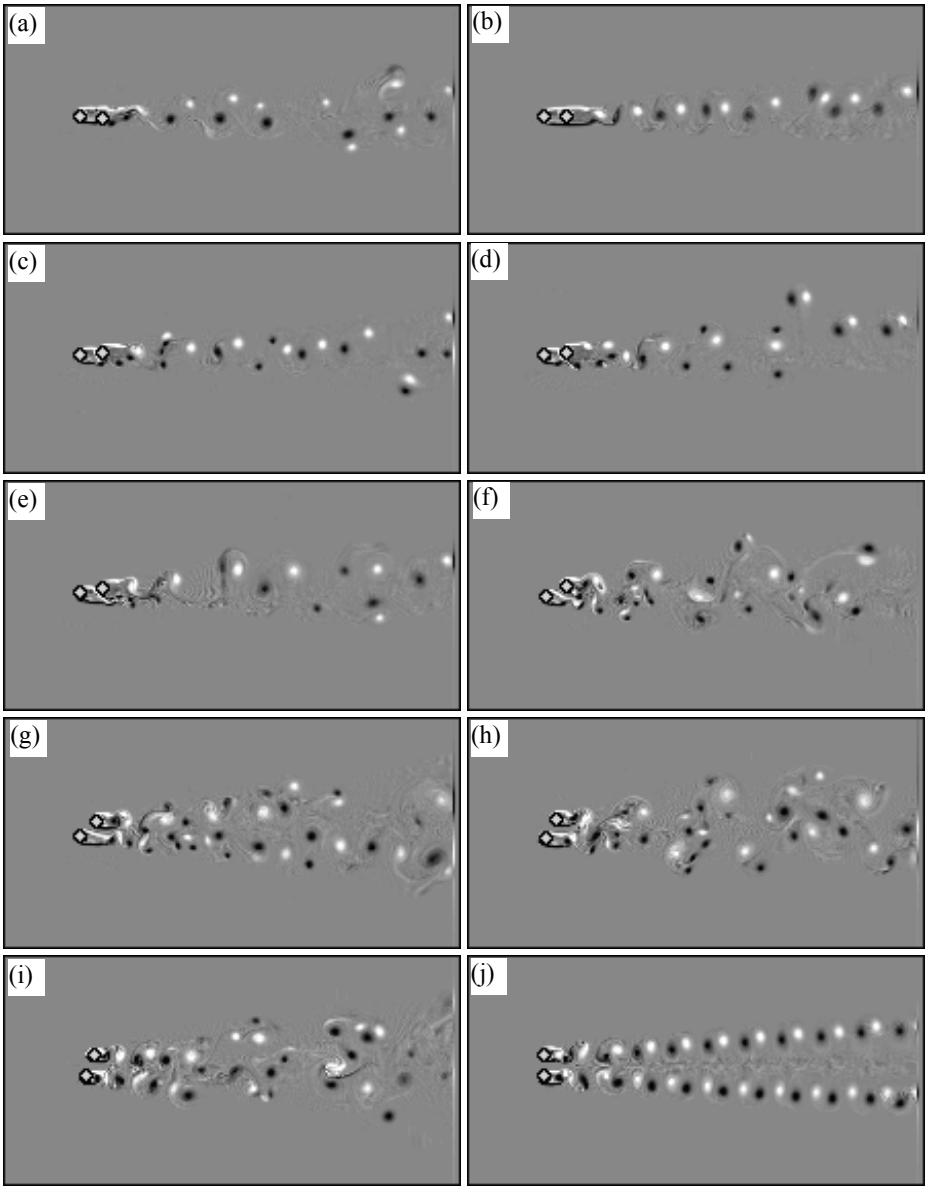

Figure 6: Vorticity contours for $Re = 72,000$: (a)$\phi = 0°$; (b)$\phi = 7°$; (c)$\phi = 9°$; (d)$\phi = 11°$; (e)$\phi = 15°$; (f)$\phi = 30°$; (g)$\phi = 45°$; (h)$\phi = 60°$; (i)$\phi = 75°$; (j)$\phi = 90°$.

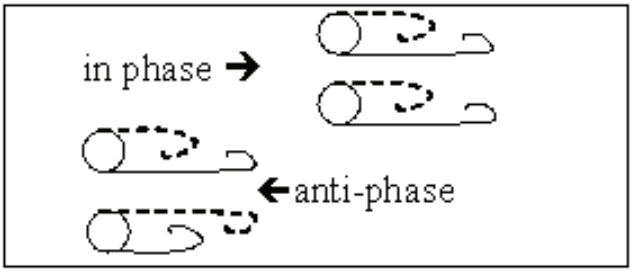

Figure 7: Illustrative scheme of vortex shedding in phase and anti-phase.

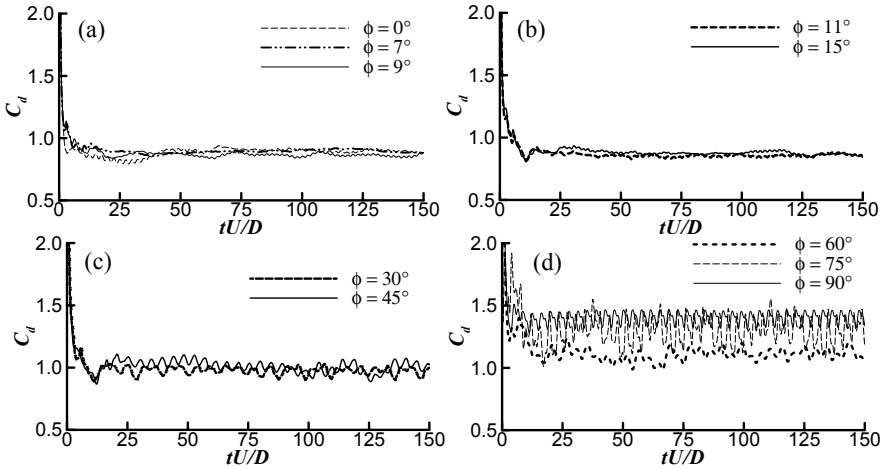

Figure 8: Time histories of C_d for the upstream cylinder (cylinder A) at $Re = 72,000$.

behavior. Increasing the angle of incidence to $\phi = 75^\circ$, the fluctuations become slightly lower than the counterparts of the upstream cylinder. For the side-by-side arrangement ($\phi = 90^\circ$), the amplitudes of the fluctuations for both cylinders are the same, as expected.

Figure 10 shows the time histories of the lift coefficient C_l for the upstream cylinder. It can be observed the small amplitudes and mean values close to zero, for $\phi < 75^\circ$. On the other hand, for $\phi \geq 75^\circ$, a considerable increase in the amplitude of the fluctuations with respect to the previous incidence angles occurs. In general, the lift coefficient history is more regular than the drag coefficient history. The mean values of C_ℓ become different from zero. By increasing the incidence angle to

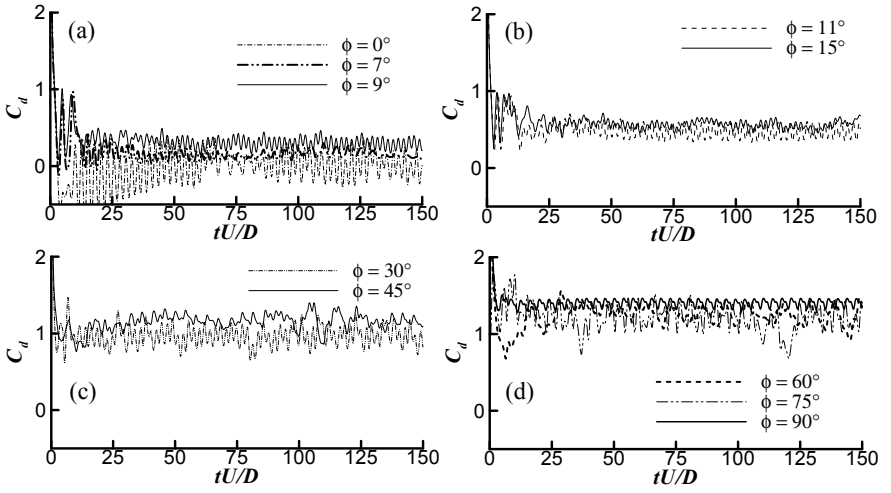

Figure 9: Time histories of C_d for the downstream cylinder (cylinder B) at $Re = 72,000$.

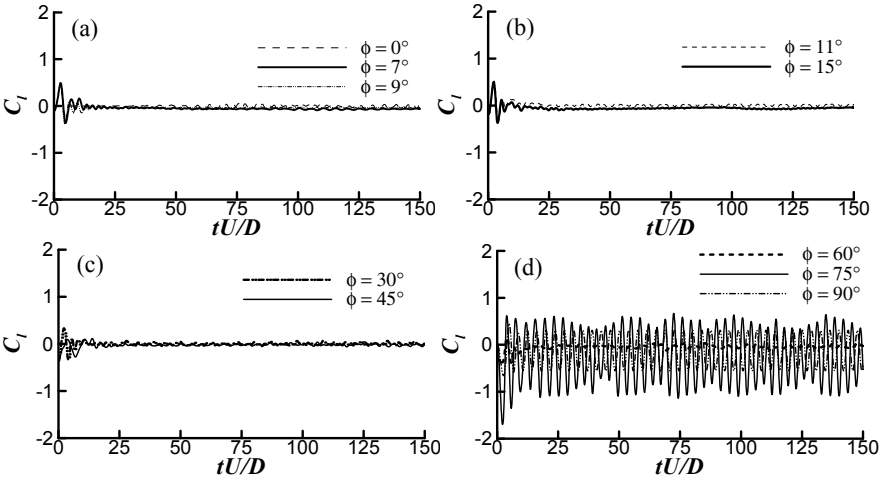

Figure 10: Time histories of C_l for the upstream cylinder (cylinder A) at $Re = 72,000$.

$\phi = 90°$, the amplitudes become slightly smaller than the amplitude for $\phi = 75°$. The phase shift observed in the time histories for $\phi = 90°$ is due to anti-phase vortex shedding.

Figure 11 shows the time history of the lift coefficient for the downstream cylinder (cylinder B). For all incidence angles, the fluctuations observed are larger than for cylinder A. It can also be noted that the amplitudes of the fluctuations increase as the incidence angle increases, and do not present null mean as noted for cylinder A for $\phi < 75°$ except for $\phi = 0°$.

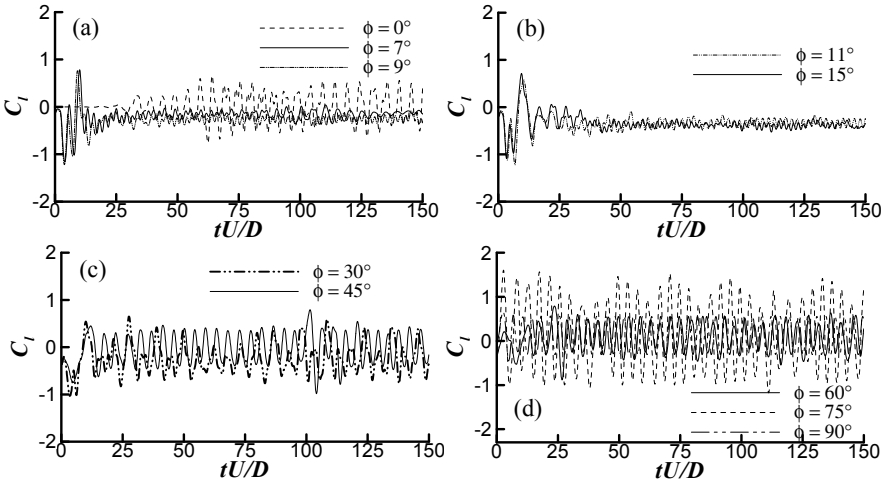

Figure 11: Time histories of C_l for the downstream cylinder (cylinder B) at $Re = 72,000$.

In the following, the mean values of the dynamic coefficients, for the upstream and downstream cylinders, are compared with the experimental results provided by [Sumner, Richards and Akosile (2005)] for pitch ratio equal to 2 and Reynolds number equal to 72,000 for different incidence angles. Figure 12(a) shows the mean values of the drag coefficient for cylinder A. For $\phi < 15°$, the C_d decreases slightly and then increases gradually with the increase of ϕ. When $\phi \leq 65°$, the mean values of the drag coefficient are smaller from that of the single cylinder ($C_d = 1.17$), with differences up to 27%. For $\phi > 65°$ the mean values of$C_d$are larger than for a single cylinder, with a maximum difference of 11%. For $\phi = 90°$, the maximum value of the drag coefficient (20% greater than to for a single cylinder) was obtained.

For the downstream cylinder (cylinder B), considered in Fig. 12(b), the mean values obtained for the drag coefficient are positive in the entire range of incidence angle

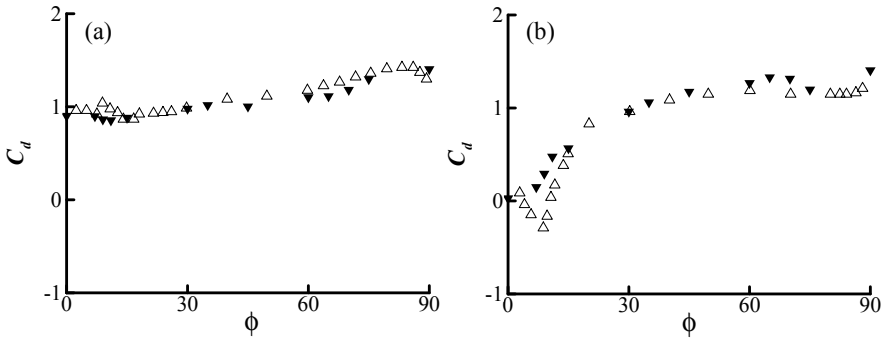

Figure 12: Mean drag coefficients versus ϕ for $Re = 72,000$: (a) cylinder A; (b) cylinder B. Full symbols: present work; empty symbols: [Sumner, Richards and Akosile (2005)].

and it increase gradually, as this angle increases. In the research work reported herein, negative values of the drag coefficient were not obtained, as opposed to what can be observed in the experimental results reported by [Sumner, Richards and Akosile (2005)].

On the other hand, for high values of ϕ, the present results show quite good agreement with the experimental results. It seems that the differences between results obtained in the two works can be reduced by the use of more accurate turbulence models, as well as by performing full three-dimensional simulations.

Figure 13 shows the mean values of the lift coefficient C_l. Figure 13(a) shows the variations of the mean values of this coefficient for the upstream cylinder, which take values close to zero, for incidence angles $\phi < 75^\circ$, and values different from zero in the range $75^\circ < \phi < 90^\circ$. On the other hand, for the downstream cylinder considered in Fig. 13(b), the mean values of the lift coefficient increase in modulus, up to $\phi = 15^\circ$. After that, the values of the mean lift coefficient decrease, in modulus, for incidence angles up to $\phi = 45^\circ$. For $\phi > 45^\circ$, the mean values of C_l are positive. Another aspect to be pointed out is that the present results for upstream cylinder are in good agreement with the corresponding acquired counterparts for the entire range of ϕ. Nevertheless, for the downstream cylinder, the agreement of the results obtained for $\phi < 15^\circ$ with those presented by [Sumner, Richards and Akosile (2005)] is not in good agreement, and further investigations are required to confirm this point.

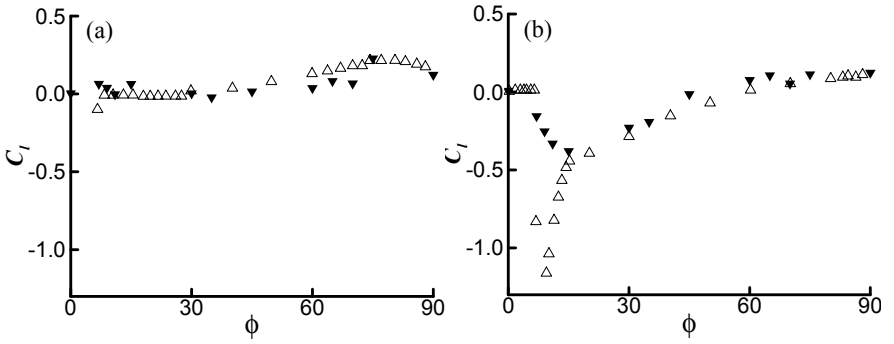

Figure 13: Mean lift coefficients versus ϕ for $Re = 72,000$: (a) cylinder A; (b) cylinder B. Full symbols: present work; empty symbols: [Sumner, Richards and Akosile (2005)].

5 Concluding remarks

In the present work, an extensive numerical investigation about interference effects between two circular cylinders in the subcritical Reynolds number regime $Re = 72,000$ was undertaken in such a way that the pair of circular cylinders of equal diameters was arranged in different configurations. The numerical results in terms of the vorticity contours, the time histories and the mean values of the dynamic coefficients were obtained for both cylinders, for a pitch ratio equal to 2 and for the incidence angle ϕ ranging from 0° to 90°. The variations of the dynamic coefficients were related to the changes in the flow patterns as change the cylinder configurations. For the tandem arrangement and $\phi = 7^\circ$, the downstream cylinder is inside the wake of the upstream cylinder. As the incidence angle increases up to 15° it was observed a new behavior in the wake. The internal shear layer from the upstream cylinder collides against the frontal part of the downstream cylinder.

For $15^\circ < \phi \leq 75^\circ$, it can be observed two wakes from the cylinders, one narrow and the other wide. For the side-by-side configuration, the wakes are independent. It was verified that these behaviors are more significant on the dynamic coefficients of the downstream cylinder as compared with the upstream cylinder.

For$\phi \leq 60^\circ$ the upstream cylinder presented mean values approximately equal to zero for the lift coefficient while for the downstream cylinder the mean values are different from zero. The results for the upstream cylinder presented good agreement with the experimental acquired counterparts obtained by [Sumner, Richards and Akosile (2005)] for all incidence angles considered herein. Nonetheless, for

the downstream cylinder the results must be improved, although they presented good agreement with experimental counterparts for $\phi > 15^{\circ}$. The difference between the numerical and experimental results can be attributed mainly to the two-dimensionality of the simulations.

Acknowledgement: The authors are deeply gratefully to the following organizations: Brazilian Research Council – CNPq for the continued support to their research work, especially through the post-doctorate scholarship granted to A.R. da Silva. Minas Gerais State Agency FAPEMIG for the financial support to their research activities and CAPES Foundation from the Brazilian Ministry of Education. Center of Research of PETROBRAS Submarine Technology – CENPES/PDP/TS for research grants and funding of their research projects.

References

Akbari, M. H.; Price, S. J. (2005): Numerical investigation of flow patterns for staggered cylinder pairs in cross-flow. *Journal of Fluids and Structures*, vol. 20, no. 4, pp. 533-554.

Báez, E.; Nicolás, A. (2009): Recirculation of Viscous Incompressible Flows in Enclosures. *CMES: Computer Modeling in Engineering & Sciences,* vol. 41, no. 2, pp. 107-130.

Carmo, B. S.; Meneghini, J. R. (2006): Numerical investigation of the flow around two circular cylinders in tandem. *Journal of Fluids and Structures*, vol. 22, no. 6, pp. 979-988.

Chorin, A. (1968): Numerical solution of the Navier-Stokes equations. *Mathematics of Computations*, vol. 22, no. 104, pp. 745–762.

Deng, J.; Ren, A. L.; Zou, J. F..; Shao, X. M. (2006): Three-dimensional flow around two circular cylinders in tandem arrangement. *Fluid Dynamics Research,* vol. 38, no. 6, pp. 386-404.

Griffith, B. E.; Peskin, S. C. (2005): On the order of accuracy of the immersed boundary method: Higher order convergence rates for sufficiently smooth problems. *Journal of Computational Physics***,** vol. 208, no. 1, pp. 75-105.

Karagoz, I.; Kaya, F. (2009): Evaluations of Turbulence Models for Highly Swirling Flows in Cyclones. *CMES: Computer Modeling in Engineering & Sciences,* vol. 43, no. 2, pp. 111-130.

Kim, D.; Choi, H. (2006): Immersed boundary method for flow around an arbitrarily moving body. *Journal of Computational Physics***,** vol. 212, no. 2, pp. 662-680.

Lee, D. S.; Ha, M. Y.; Yoon, H. S.; Balachandar, S. (2009): A numerical study on the flow patterns of two oscillating cylinders. *Journal of Fluids and Structures*, vol. 25, no. 2, pp. 263-283.

Lima e Silva, A. L. F.; Silveira-Neto, A.; Damasceno, J. J. R. (2003): Numerical Simulation of Two Dimensional Flows over a Circular Cylinder using the Immersed Boundary Method. *Journal of Computational Physics,* vol. 189, no. 2, pp. 351-370.

Liu, D.; Yu, D. (2008): The Coupling Method of Natural Boundary Element and Mixed Finite Element for Stationary Navier-Stokes Equation in Unbounded Domains. *CMES: Computer Modeling in Engineering & Sciences,* vol. 37, no. 3, pp. 305-329.

Meitz, H. L.; Fasel, H.F. (2000): A compact-different scheme for the Navier-Stokes equations in vorticity-velocity formulation. *Journal of Computational Physics,* vol. 157, no. 1, pp. 371-403.

Mittal, S. (2008): Linear Stability Analysis of Time-Averaged Flow Past a Cylinder. *CMES: Computer Modeling in Engineering & Sciences,* vol. 27, no. 2, pp. 63-78.

Naudascher, E.; Rockwell, D. (1994): *Flow-Induced Vibrations*: *An Engineering Guide*, Dover Publications, Inc. Mineola, New York, 414p.

Nicolás, A.; Bermúdez, B. (2007): Viscous Incompressible Flows by the Velocity-Vorticity Navier-Stokes Equations. *CMES: Computer Modeling in Engineering & Sciences,* vol. 20, no. 2, pp. 73-83.

Peskin, C. S. (1977): Numerical Analysis of Blood Flow in the Heart. *Journal of Computational Physics*, vol. 25, no. 3, pp. 220-252.

Peskin, C. S.; McQueen, D. M. (1994): A General Method for the Computer Simulation of Biological Systems Interacting with Fluids. *SEB: Symposium on Biological Fluid Dynamics*, Leeds, England, July 5-8.

Schneider, G. E.; Zedan, M. A. (1981): A modified strongly implicit procedure for the numerical solution of field problems. *Numerical Heat Transfer,* vol. 4, no. 1, pp. 1-19.

Smagorinsky, J. (1963): General Circulation Experiments with Primitive Equations. *Mon. Weather Rev*, v. 91, pp. 99-164.

Su, S.W.; Lai, M.C.; Lin, C.A. (2007): An immersed boundary technique for simulating complex flows with rigid boundary. *Computers & Fluids,* vol. 36, no. 2, pp. 313-324.

Sumner, D.; Price, S. J.; Païdoussis, M. P. (1999): Tandem cylinders in impulsively started flow. *Journal of Fluids and Structures*, vol. 13, no. 7, pp. 955-965.

Sumner, D.; Richards, M. D.; Akosile, O.O. (2005): Two staggered circular cylinders of equal diameter in cross-flow. *Journal of Fluids and Structures*, vol. 20, no. 2, pp. 255-276.

Vertnik, R.; Šarler, B. (2009): Solution of Incompressible Turbulent Flow by a Mesh-Free Method. *CMES: Computer Modeling in Engineering & Sciences,* vol. 44, no. 1, pp. 65-95.

Wang, Z. J.; Zhou, Y. (2005): Vortex interactions in a two side-by-side near-wake. *International Journal of Heat and Fluid Flow*, vol. 26, no. 3, pp. 362-377.